PROJECT 1: MUON COLLIDER

FYS5555 - RESEARCH-BASED PARTICLE PHYSICS

ELISABETH CHRISTENSEN

1. TRANSITION AMPLITUDES

The contributions to the process $\mu^+\mu^- \to b\bar{b}$ includes the propagator for QED (γ) as well as the propagators for the electroweak theory (Z) and Higgs (H). The Feynman diagrams for each of these processes can be seen in figure 1. We know that the total amplitude $\langle|M_{tot}|^2\rangle$ is a sum of the amplitudes for each individual process including interference terms, and can be expressed as

$$\langle|M_{tot}^2|\rangle = \langle|M_\gamma|^2\rangle + \langle|M_Z|^2\rangle + \langle|M_H|^2\rangle + 2\langle M_\gamma^\dagger M_Z\rangle + 2\langle M_\gamma^\dagger M_H\rangle + 2\langle M_Z^\dagger M_H\rangle \tag{1}$$

From figure 1 we can derive the transition amplitude for each process:

$$\begin{aligned}
-iM_\gamma =& -i\frac{e^2}{3s}[\overline{v}^{s'}(p_2)\gamma^\mu u^s(p_1)][\overline{u}^r(p_3)\gamma_\mu v^{r'}(p_4)] \\
-iM_Z =& i\frac{g_Z^2}{s-m_Z^2+im_Z\Gamma_Z}[\overline{v}^{s'}(p_2)\frac{1}{2}\gamma^\mu(c_V-c_A\gamma^5)u^s(p_1)] \\
&\times[\overline{u}^r(p_3)\frac{1}{2}\gamma_\mu(\tilde{c}_V-\tilde{c}_A\gamma^5)v^{r'}(p_4)] \\
-iM_H =& -i\frac{m_\mu m_b g_W^2}{2m_W(s-M_H^2+im_H\Gamma_H)}[\overline{v}^{s'}(p_2)u^s(p_1)][\overline{u}^r(p_3)v^{r'}(p_4)]
\end{aligned} \tag{2}$$

where $s=(p_1+p_2)^2$, $e^2=4\pi\alpha$ and $\Gamma_Z=2.4952$ and $\Gamma_H=0.00407$. c_V, c_A, $\tilde{c}_V$, $\tilde{c}_A$ are the vector and axial vector couplings to Z of respectively μ^- and b, and can be found in table 1.[1]

2. DIFFERENTIAL CROSS SECTION

The spin-averaged square amplitude can be expressed as

$$\langle|M_{tot}|^2\rangle = \frac{1}{4}\sum_{\text{spins}}|M_{tot}|^2 \tag{3}$$

Date: March 2, 2020.

[1] All measured variables used in this report such as the coupling constants, decay widths and masses of the particles can be found at http://pdg.lbl.gov/ ([1, 2])

	m[GeV]
e	0.511
μ	0.106
c	1.275
b	4.180
Z	91.188
H	125.180

	Q_f	c_V	c_A
e^-, μ^-, τ^-	-1	-0.04	$-\frac{1}{2}$
u, c, t	$+\frac{2}{3}$	+0.19	$+\frac{1}{2}$
d, s, b	$-\frac{1}{3}$	-0.35	$-\frac{1}{2}$

TABLE 1. Measurements of particles used. The vector and axial vector couplings to the Z is measured by assuming $sin^2\theta_W = 0.231$ [2].

such that the spin-averaged square amplitudes for the individual theories are

$$\langle|M_H|^2\rangle = \frac{m_b^2 m_\mu^2 g_W^4}{4[(s-m_H^2)^2+m_H^2\Gamma_H^2]}[(p_1\cdot p_2)(p_3\cdot p_4) - m_b^2(p_1\cdot p_2) - m_\mu^2(p_3\cdot p_4) + m_\mu^2 m_b^2] \tag{4}$$

$$\langle|M_\gamma|^2\rangle = \frac{8e^4}{9s^2}[(p_1\cdot p_4)(p_2\cdot p_3) + (p_1\cdot p_3)(p_2\cdot p_4) + m_b^2(p_1\cdot p_2) + m_\mu^2(p_3\cdot p_4) + 2m_b^2 m_\mu^2] \tag{5}$$

$$\begin{aligned}\langle|M_Z|^2\rangle = \frac{g_Z^4}{2[(s-m_Z^2)^2+m_Z^2\Gamma_Z^2]}\{&(c_V^2+c_A^2)(\tilde{c}_V^2+\tilde{c}_A^2)[(p_1\cdot p_4)(p_2\cdot p_3)+(p_1\cdot p_3)(p_2\cdot p_4)]\\ &+m_b^2(c_V^2+c_A^2)(\tilde{c}_V^2-\tilde{c}_A^2)(p_1\cdot p_2)\\ &+m_\mu^2(c_V^2-c_A^2)(\tilde{c}_V^2+\tilde{c}_A^2)(p_3\cdot p_4)\\ &-4c_V c_A c\tilde{c}_V\tilde{c}_A[(p_1\cdot p_4)(p_2\cdot p_3)-(p_1\cdot p_3)(p_2\cdot p_4)]\\ &+2m_\mu^2 m_b^2(c_V^2-c_A^2)(\tilde{c}_V^2-\tilde{c}_A^2)\}\end{aligned} \tag{6}$$

where the derivation for each individual spin-averaged square amplitude can be seen separately in the attachments.

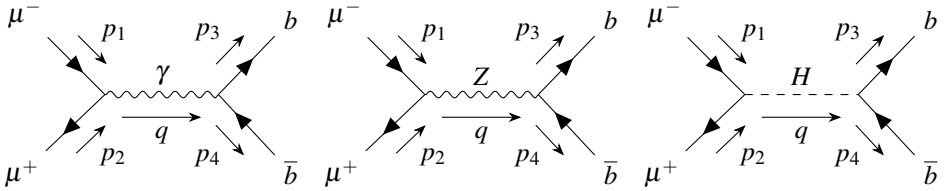

FIGURE 1. Feynman diagrams for the process $\mu^+\mu^- \to b\bar{b}$

The spin-averaged square amplitudes can be used to calculate the differential cross section in the center-of-mass frame, which can be expressed as

$$\frac{d\sigma}{d(\cos\theta)} = 3\times\frac{1}{32\pi s}\frac{p_f^*}{p_i^*}\langle|M|^2\rangle \tag{7}$$

where p_f^* and p_i^* are respectively the magnitude of the final and initial particle states in the center-of-mass frame. A factor of 3 is included to describe the additional three colour charges $r\bar{r}$, $b\bar{b}$ and $g\bar{g}$ for the quarks in the final state. Thus, the differential cross sections for each individual propagator including H, γ and Z (excluding the interference terms) at a center-of-mass energy $\sqrt{s} = 150$ GeV can be seen in figure 3. Here, we see that the most dominating contributions are that of QED and Z, whereas the process including Higgs as the propagator is nearly zero. Thus, we can choose to neglect the Higgs process in the rest of the calculations of the total amplitude squared, allowing us

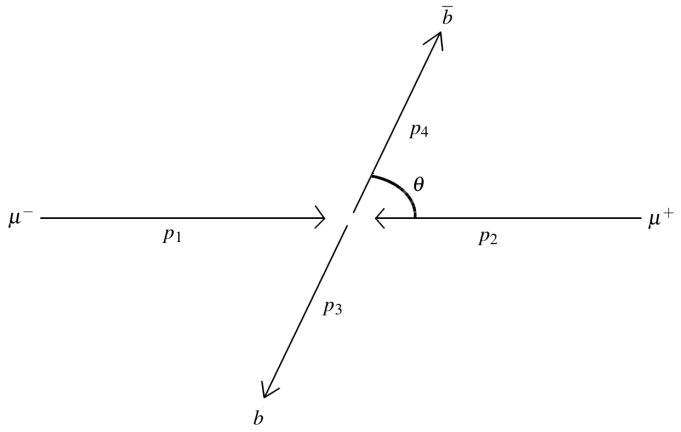

FIGURE 2. Collision in the center-of-mass frame

to rewrite eq. (1) as

$$
\begin{aligned}
(8)\quad \langle|M_{tot}|^2\rangle =& \langle|M_\gamma|^2\rangle + \langle|M_Z|^2\rangle + 2\langle M_\gamma^\dagger M_Z\rangle \\
=& \frac{8e^4}{9s^2}[(p_1\cdot p_4)(p_2\cdot p_3)+(p_1\cdot p_3)(p_2\cdot p_4)+m_b^2(p_1\cdot p_2)+m_\mu^2(p_3\cdot p_4)+2m_b^2m_\mu^2] \\
&+\frac{g_Z^4}{2[(s-m_Z^2)^2+m_Z^2\Gamma_Z^2]}\{(c_V^2+c_A^2)(\tilde{c}_V^2+\tilde{c}_A^2)[(p_1\cdot p_4)(p_2\cdot p_3)+(p_1\cdot p_3)(p_2\cdot p_4)] \\
&+m_b^2(c_V^2+c_A^2)(\tilde{c}_V^2-\tilde{c}_A^2)(p_1\cdot p_2)+m_\mu^2(c_V^2-c_A^2)(\tilde{c}_V^2+\tilde{c}_A^2)(p_3\cdot p_4) \\
&-4c_Vc_Ac\tilde{c}_V\tilde{c}_A[(p_1\cdot p_4)(p_2\cdot p_3)-(p_1\cdot p_3)(p_2\cdot p_4)]+2m_\mu^2m_b^2(c_V^2-c_A^2)(\tilde{c}_V^2-\tilde{c}_A^2)\} \\
&+2\times\frac{4e^2g_Z^2}{3s(s-m_Z^2+im_Z\Gamma_Z)}\{c_V\tilde{c}_V[(p_1\cdot p_4)(p_2\cdot p_3)-(p_1\cdot p_3)(p_2\cdot p_4)] \\
&-c_A\tilde{c}_A[(p_1\cdot p_3)(p_2\cdot p_4)-(p_1\cdot p_4)(p_2\cdot p_3)] \\
&+c_Vc_Vm_b^2(p_1\cdot p_2)-c_V\tilde{c}_Vm_\mu^2(p_3\cdot p_4)+2c_V\tilde{c}_Vm_\mu^2m_b^2\}
\end{aligned}
$$

The momentas in the center-of-mass frame, as seen in figure 2, can be expressed as

$$(9)\qquad p_1=(E,0,0,p),\quad p_3=(E,-p'\sin\theta,0,-p'\cos\theta)$$

$$(10)\qquad p_2=(E,0,0,-p),\quad p_4=(E,p\sin\theta,0,p'\cos\theta)$$

$$(11)\qquad s=(p_1+p_2)^2=4E^2$$

$$(12)\qquad p_1\cdot p_2=E^2+p^2,\quad p_1\cdot p_3=p_2\cdot p_4=E^2+pp'\cos\theta$$

$$(13)\qquad p_3\cdot p_4=E^2+p'^2, p_1\cdot p_4=p_2\cdot p_3=E^2-pp'\cos\theta$$

where $p=\sqrt{E^2-m_\mu^2}$ and $p'=\sqrt{E^2-m_b^2}$.

The differential cross-section, when plugging the momentas defined above into the results from eq. (8), can be seen in figure 4. Here, there is almost a complete overlap between the analytical

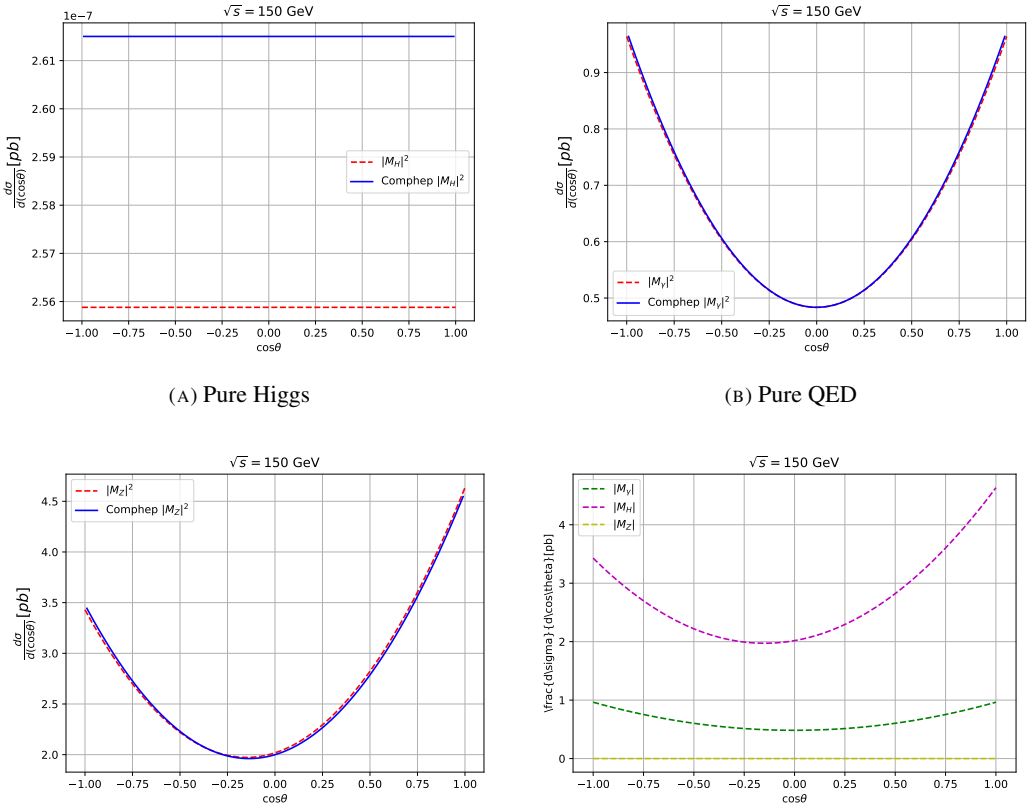

(A) Pure Higgs

(B) Pure QED

(C) Pure Z

(D) Pure QED, Z, Higgs

FIGURE 3. Differential cross-sections, excluding interference terms, compared with CompHep

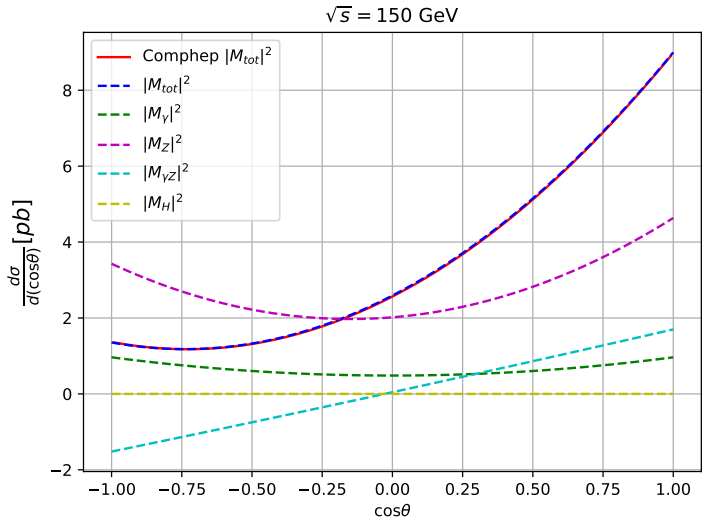

FIGURE 4. Differential cross section compared with CompHep

calculations and the numerical calculations as derived from CompHep. We also see that the interference term along with the pure QED term clearly also has an affect at $\langle|M_{tot}|^2\rangle$, although their contributions are smaller than that of pure Z.

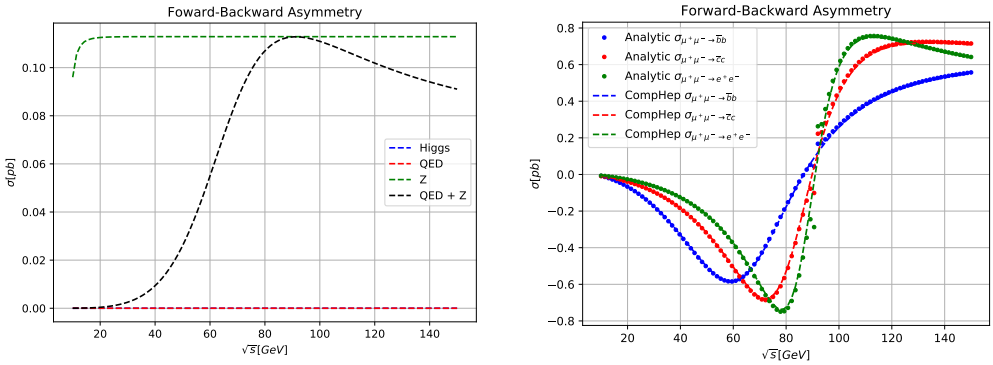

(A) Asymmetry for individual processes for final state $b\bar{b}$

(B) Asymmetry for different final states $b\bar{b}$, $c\bar{c}$ and e^+e^-

FIGURE 5. Forward-Backward asymmetry

3. FORWARD-BACKWARD ASYMMETRY

Forwards-backwards asymmetry can be expressed as

$$\sigma_{FB} = \frac{N_{\theta<\pi/2} - N_{\theta>\pi/2}}{N_{\theta>\pi/2} + N_{\theta<\pi/2}} = \frac{\sigma_{\theta<\pi/2} - \sigma_{\theta>\pi/2}}{\sigma_{\theta>\pi/2} + \sigma_{\theta<\pi/2}} \tag{14}$$

where $N_{\theta<\pi/2}$ and $N_{\theta>\pi/2}$ stands for the amount of events scattering respectively in the forward direction and in the backward direction. The cross-section in the forward direction ($\sigma_F = \sigma_{\theta<\pi/2}$) and in the backward direction ($\sigma_B = \sigma_{\theta>\pi/2}$) can be expressed as

$$\sigma_F \equiv 2\pi \int_0^1 \frac{d\sigma}{d\Omega} d(cos\theta), \qquad \sigma_B \equiv 2\pi \int_{-1}^0 \frac{d\sigma}{d\Omega} d(cos\theta) \tag{15}$$

Integrating eq. (8) with respect to $\cos\theta \in [-1,1]$ using the trapezoidal rule, as provided by Python, multiplying by 2π, and from there on following the definitions in eq. (14) and (15), we obtain the asymmetries of the different processes as shown in figure 5a. Here, we see that the asymmetry of the pure QED alone is nearly negligible, meaning that the angular distribution of the final-state leptons is fairly symmetric, as can also be seen in figure 3b. However, the asymmetry of the pure Z-channel is more prominent, and a bit more skewed as can also be seen in figure 3c. Whereas the contribution from Higgs is zero due to remaining constant throughout the different scattering angles, which we can also see from the angular distribution of figure 3a. Looking at the total asymmetry from fig. 5b of the final-state quarks $b\bar{b}$, σ_{FB} is approximately zero for $\sqrt{s} < 10$GeV, which is due to the QED term being the most dominating at small energies as well as symmetric in the angular distribution. As we move a bit higher up on the energy scale, σ_{FB} becomes negative, meaning that the cross-sections for backward scattering at $\theta > \pi/2$ is much more likely than scattering at $\theta < \pi/2$ when $\sqrt{s} \in (10,90)$GeV. If we move to higher energies, forward scattering at $\theta < \pi/2$ starts to dominate due to the contribution from the Z term. Close to m_Z the asymmetry is about zero. The angular distribution of the final-state $b\bar{b}$ compared to the final states $c\bar{c}$ and e^+e^- appears to be more shifted than that of the two latter cases. This may be due to the vector coupling c_V being greater for $b\bar{b}$ than e^+e^- and $c\bar{c}$.

4. TOTAL CROSS SECTION

Inserting the momentas defined in eqs. (9)-(13) into the total amplitude of eq. (8), and integrating over $\cos\theta \in [-1,1]$ using the trapezoidal rule, we get the total cross sections as seen in figure 6. Looking at fig. 6a the total cross section is dominated by QED at lower energy scales due to the fact that the center-of-mass energy $\sqrt{s}$ is not yet high enough to produce a Z as a propagator. As $\sqrt{s}$ increases, the production of a Z-boson becomes more and more likely until the pure Z-channel

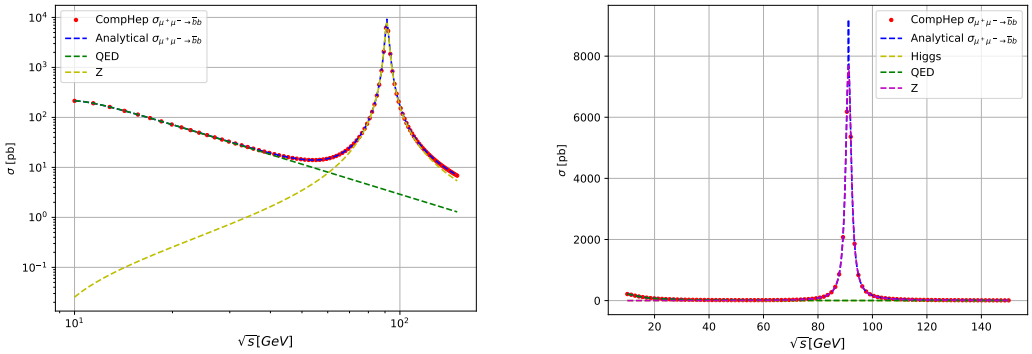

(A) Logarithmic scale (B) Linear scale

FIGURE 6. Total cross section

starts to dominate over γ which leaves us with a maximum when $\sqrt{s}$ approaches m_Z. This can also be seen in the linear plot of figure 6b where there is a resonant peak at $\sqrt{s} \approx m_Z$.

5. NEW PHYSICS

We can introduce a new gauge boson Z' to CompHep by assuming the same interactions as Z in the Electroweak theory, only at a substantially higher mass. It is postulated [1] that the mass of the Z'-boson has a lower bound of 4.5 TeV in the Standard Model, with CL = 95%, through a pp direct search. Thus, we can set the mass of our hypothetical gauge boson at say $m_{Z'} = 5.0$ TeV.

5.1. **Differential cross section.** When including the Z'-boson into our theory, our total amplitude squared now becomes

$$\langle |M_{tot}|^2 \rangle = \langle |M_\gamma|^2 \rangle + \langle |M_Z|^2 \rangle + \langle |M_{Z'}|^2 \rangle + 2\langle M_\gamma^\dagger M_Z \rangle + 2\langle M_\gamma^\dagger M_{Z'} \rangle + 2\langle M_Z^\dagger M_{Z'} \rangle \tag{16}$$

Calculating the differential cross-section at $\sqrt{s} = 15$ TeV and plotting using CompHep, we get the plot as shown in figure 7, where $d\sigma/d(\cos\theta)$ is plotted with respect to all processes. We see that at higher energies Z and γ becomes more and more suppressed in comparison to Z'. However, the total differential cross section is on the order of 10^4 times smaller than that of the differential cross section from figure 4. This is due to the high energies involved as can be seen from the amplitudes in (2), where each process is inversely proportional to s at high energies (i.e. when the mass and decay width of Z is nearly negligible).

5.2. **Total cross section.** Integrating the differential cross section over $\cos\theta \in [-1, 1]$ we get the total cross section as seen in figure 8. Here, we clearly see a resonant peak at $m_{Z'}$ as we would expect.

5.3. **Forward-backward asymmetry.** The forward-backward asymmetry for the process $\mu^+\mu^- \longrightarrow b\bar{b}$ when including Z' can be seen in figure 9. Here, it seems as though forward scattering at $\theta < \pi/2$ is dominant at energies below roughly 1.4 TeV and above 1.9 TeV, while backward scattering at $\theta > \pi/2$ mostly happens when $\sqrt{s} \in (1.4, 1.9)$ TeV.

6. ATLAS DATA ANALYSIS

Using the 8TeV dataset as published by ATLAS OpenData, we can plot the invariant mass m_{ll} for possible processes leading to dilepton final states. The OpenData considers the process

$$pp \longrightarrow l^+l^-,$$

where we will be looking at processes with lepton pairs of e^+e^- and $\mu^+\mu^-$ in the final state.

In doing so, we end up with the stacked histograms as shown in figure 10. For the individual processes we see that the expected contribution for Higgs (through Monte Carlo simulations) is fairly low, whereas the process including Z are the most dominating ones above ~ 25 GeV. We also see that Drell-Yan processes, i.e. $q\bar{q} \longrightarrow l^+l^-$, are mostly present at energies below 25 GeV. We

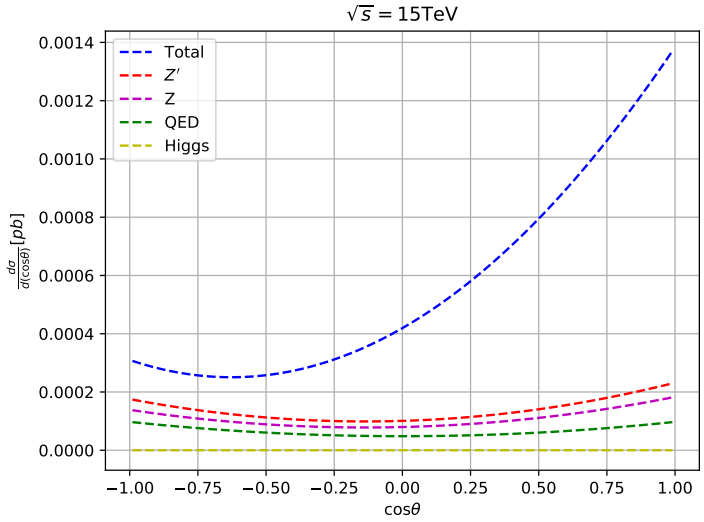

FIGURE 7. Differential cross section when including SM Z' for the process $\mu^+\mu^- \longrightarrow b\bar{b}$ using CompHep

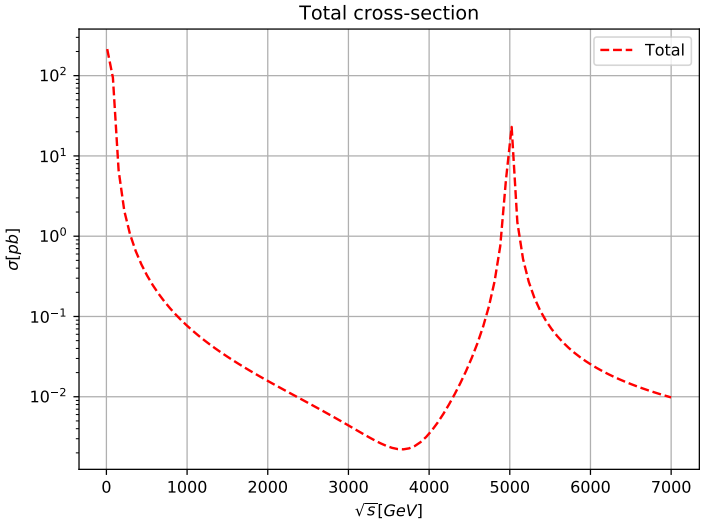

FIGURE 8. Total cross section when including SM Z' for the process $\mu^+\mu^- \longrightarrow b\bar{b}$ using CompHep

also see a resonant peak about the $Z-$mass $m_Z = 91.2$ GeV, as one would expect from the theory.

The Github repository for this project can be found at *https://github.com/elisabethchr/FYS5555* which includes the code and data used for the analysis of the invariant mass of dileptons.

REFERENCES

[1] M. Tanabashiet al.(Particle Data Group), Phys. Rev. D98, 030001 (2018) and 2019 update
[2] Thomson, M., 2013, *Modern Particle Physics*, Cambridge University Press, Cambridge

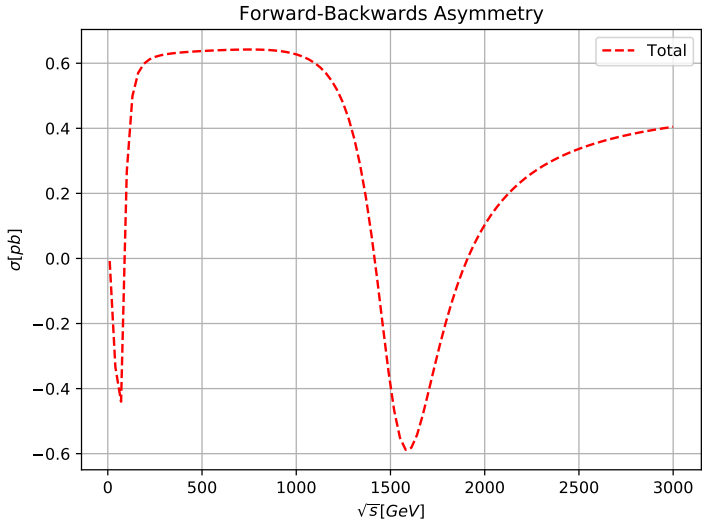

FIGURE 9. Forward-backward asymmetry when including SM Z' for the process $\mu^+\mu^- \longrightarrow b\bar{b}$ using CompHep

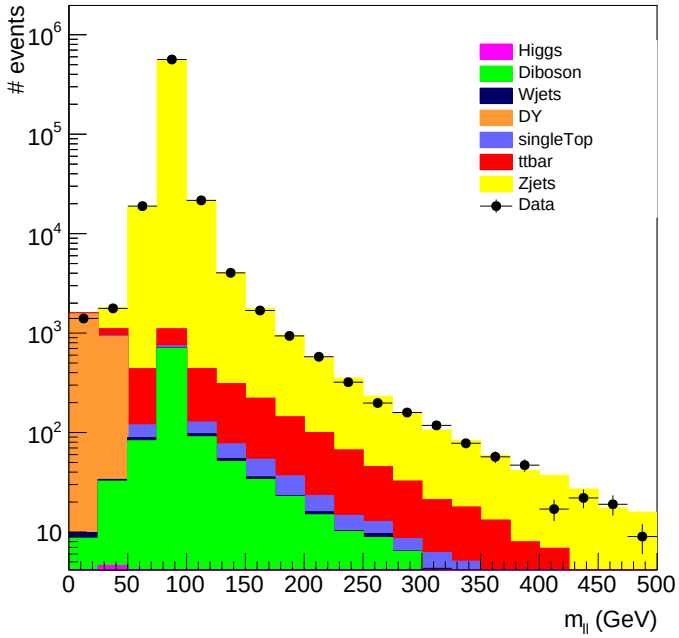

FIGURE 10. Invariant mass distributions for dileptons using the 8 TeV dataset provided by ATLAS OpenData